



## Research paper

## Highly selective oxidation of furfuryl alcohol over monolayer titanate nanosheet under visible light irradiation



Hao Wang<sup>a</sup>, Yujie Song<sup>a</sup>, Jinhua Xiong<sup>a</sup>, Jinhong Bi<sup>a</sup>, Liuyi Li<sup>b</sup>, Yan Yu<sup>b</sup>, Shijing Liang<sup>a,\*</sup>, Ling Wu<sup>a,\*</sup>

<sup>a</sup> State Key Laboratory of Photocatalysis on Energy and Environment, Fuzhou University, Fuzhou, 350116, China

<sup>b</sup> Key Laboratory of Eco-Materials Advanced Technology (Fuzhou University), Fujian Province University, 350116, China

## ARTICLE INFO

## Keywords:

Monolayer nanosheet  
Furaldehyde  
Visible light  
Photocatalysis  
Surface coordination species

## ABSTRACT

Monolayer  $H_{1.4}Ti_{1.65}O_4\cdot H_2O$  nanosheet (denoted as NST) has been prepared as a photocatalyst for the oxidation of furfuryl alcohol (denoted as FA) to furaldehyde under visible light irradiation. The photocatalytic activity of NST is over 10 times higher than that of its layered counterpart. This enhanced activity may be attributed to the high percentage of exposed Lewis acid sites in NST. The in-situ FTIR result suggests that FA are efficiently chemisorbed on the exposed Lewis acid sites forming the surface coordination species via C–O groups, resulting in the activation of FA. The surface coordination species would respond to visible light absorption. Furthermore, The XAFS result shows that the signals for Ti–O and Ti–Ti in NST are weaker dramatically and the signals positions are shifted by 0.03 Å in the higher R direction as compared with those in layered counterpart, suggesting the more exposed Ti and O defects in NST. The oxygen molecules absorbed on these surface defects are activated forming  $\cdot O_2^-$  by photo-electrons under visible light irradiation. Finally, a possible mechanism has been proposed at a molecular level.

## 1. Introduction

Aldehydes are of high industrial importance because of its use as an intermediate in the production of fine chemicals. Photocatalytic selective oxidation of alcohols to aldehydes by utilizing light energy has attracted wide attentions. They provide the possibility to using the green and renewable energy [1–3]. In the last several decades, massive photocatalysts (such as  $C_3N_4$  [4],  $WO_3$  [5],  $CdS$  [6] and  $TiO_2$  [7]) have been developed for the oxidation the alcohols to obtaining the corresponding aldehydes. Up to now, the benzaldehyde, cinnamyl aldehyde, 2-thiophenecarboxaldehyde and so on have been synthesized efficiently via the selective oxidation of corresponding alcohols under the light irradiation [8–10]. However, the fact is that the furfuraldehyde, a key chemical product that widely used in synthetic plastics, pharmaceuticals, pesticides and other industries, are few studied in present photocatalytic system [11,12]. The developed catalytic system contributes to the selective oxidation of FA to furaldehyde. But, the low conversion of FA and the inferior furaldehyde selectivity lead to the materials waste and impurity product [13]. These limit their applications in general. Moreover, the elevated temperature results in the extra energy consuming [14]. Therefore, the development of the suitable photocatalysts with atom-efficiency and cost/energy savings for

efficiently catalytic selective oxidation of FA to furaldehyde is a pressing matter of the moment.

Monolayer metal oxide nanosheet has attracted great attention due to their atomic thickness, high carrier mobility, the formation of dangling bonds and large surface area [15,16]. These unique properties endow the monolayer nanosheet the promising applications in selectivity oxidation of alcohols to aldehydes [17,18]. Analogously, the  $H_{1.4}Ti_{1.65}O_4\cdot H_2O$  nanosheet is a lepidocrocite-type photocatalysts that consists of a polyanion layer built by a distorted  $TiO_6$  octahedra flat and many defects. The thickness of monolayer  $H_{1.4}Ti_{1.65}O_4\cdot H_2O$  nanosheet is only 1.2 nm. Thus, a great deal of unsaturated surface metal sites (USMSs) can be fully exposed in the monolayer nanosheet, acting as the Lewis acid sites [19,20]. In the catalytic reactions, the USMSs can interact with the FA intimately. And then, the FA molecules would be activated. This is a very important step in the oxidation of FA. Therefore,  $H_{1.4}Ti_{1.65}O_4\cdot H_2O$  nanosheet could offer a more sustainable and environmentally friendly alternation to the traditional catalytic system for the selective oxidation of FA to furaldehyde. Furthermore, one of the principal issues is where and how the FA molecules bind in the surface of monolayer nanosheet. In addition, the surface defective sites make the detailed understanding of FA molecules absorbed behavior very challenging.

\* Corresponding authors.

E-mail addresses: [sjliang2011@gmail.com](mailto:sjliang2011@gmail.com) (S. Liang), [wuling@fzu.edu.cn](mailto:wuling@fzu.edu.cn) (L. Wu).

Herein, we prepared the monolayer NST for photocatalytic selective oxidation of FA molecules to furaldehyde for the first time. The surface Lewis acid sites, defects and electron structures in NST have been thoroughly studied by X-ray absorption fine structure (XAFS) and in-situ ESR spectroscopy. Moreover, the interactions between FA molecules and these special surface sites have been fully revealed by in situ molecular spectra. Based on the exhaustive characterizations, a surface coordination species between FA and NST was proposed to explain the promoted catalytic performance. Additionally, the photoelectron-chemical measurements have been also investigated to illuminate the effects of charge transport on the photocatalytic transformation efficiency. Finally, a surface coordination species promoted photocatalytic mechanism for the oxidation of FA under visible light irradiation has been revealed at a molecular level.

## 2. Experimental section

### 2.1. Reagents and chemicals

All the reagents were analytical grade purchased from Alfa Aesar China Co., Ltd, such as hydrochloric acid (HCl, 40%), tetrabutylammonium (TBAOH) hydroxide (40 wt% solution) solution, titanium oxide ( $\text{TiO}_2$  anatase), cesium carbonate ( $\text{Cs}_2\text{CO}_3$ , 99%), zinc oxide ( $\text{ZnO}$ ), Furfuryl alcohol (98%) and 2-furaldehyde (98%).

### 2.2. Catalyst preparation

The preparation procedures of the catalysts have been illustrated in Fig. S1. Firstly, zinc-doped titanate  $\text{Cs}_x\text{Ti}_{2-x}/\text{Zn}_{x/2}\text{O}_4$  ( $x = 0.7$ ) was prepared by a high temperature solid state reaction method [21]. A mixture of  $\text{Cs}_2\text{CO}_3$ ,  $\text{ZnO}$ , and  $\text{TiO}_2$  with a molar ration of 1:1:4.7 was placed in an alumina crucible. Then, the mixture was heated in air at 800 °C for 2 h, followed by calcined at 1000 °C for 20 h. The obtained sample ( $\text{Cs}_{0.7}\text{Ti}_{1.65}\text{Zn}_{0.35}\text{O}_4$ ) was denoted as SSR. The layered  $\text{H}_{1.4}\text{Ti}_{1.65}\text{O}_4\text{H}_2\text{O}$  (denoted as LAT) was prepared by a protonic exchange. For a typical reaction, SSR was stirred in a 1 M HCl solution at room temperature for 5 days. The acidic solution was renewed every day to promote a complete ionic exchange. After the protonic exchange reaction, intercalation of organic amines was processed by dispersing 4 g of LAT into 1000 mL of TBAOH aqueous solutions with vigorously shaking for more than 5 days at the ambient temperature. The resulting colloidal suspensions were dealt with 1 M HCl solution. The obtained solid product was separated from the suspension by centrifugation. The sample was washed by deionized water. The final sample was dried in an oven at 60 °C overnight denoted as NST.

### 2.3. Catalyst characterization

Structural analysis of the synthetic samples was carried out by powder X-ray diffraction (XRD) on a Bruker D8 Advance X-ray diffractometer operated at 40 kV and 40 mA with Ni-filtered Cu K $\alpha$  radiation ( $\lambda = 1.5406 \text{ \AA}$ ). UV-vis diffuse reflectance spectra (UV-vis DRS) were recorded by using a UV-vis spectrophotometer (Varian Cary 500) in which  $\text{BaSO}_4$  powder was used as a reference. The data were converted to Kubelka-Munk (KM) functions. Nitrogen adsorption – desorption isotherms were measured on an ASAP 2020 M apparatus (Micromeritics Instrument Corp., USA). The sample was degassed in vacuum at 120 °C for 6 h and then analyzed at –196 °C. The morphologies and structures of the samples were examined by scanning electron microscopy (FEI Nova NANO-SEM 230 spectrophotometer). The transmission electron microscopy (TEM) and the high resolution transmission electron microscopy (HRTEM) analysis were taken by FEI model Tecnai G2 F20 S-TWIN instrument. Atomic force microscope (AFM) images were collected on a Nanoscope E multimode. The NST colloid was diluted for preparation of AFM measurement. 4  $\mu\text{l}$  of the suspension was dispersed on the mica plate. After air drying naturally,

the sample was used to measure the thickness of the NST. X-ray photoelectron spectroscopy (XPS) measurements were carried out by using a PHI Quantum 2000 XPS system with a monochromatic Al K $\alpha$  source and a charge neutralizer. All of the binding energies were calibrated by the C1 s peak at 284.6 eV. The electron spin resonance (ESR) signals were recorded with a Bruker A300 spectrometer at room temperature using a 300 W Xe lamp (Beijing Trustech, PLS-SXE300c) as light source.  $^1\text{H}$  nuclear magnetic resonance (NMR) spectra were measured at room temperature using a Bruker MSL400 spectrometer. Fourier transform infrared (FT-IR) data were recorded for samples prepared via the standard KBr technique on a PerkinElmer Spectrum 2000 FT-IR spectrometer. The in-situ infrared spectra of pyridine adsorbed on the catalysts were obtained at a resolution of 4  $\text{cm}^{-1}$ . A total of 64 scans were performed to obtain each spectrum. Firstly, the powder samples were first pressed into a self-supporting IR disk (18 mm diameter, 10 mg), then the disk was placed into the sample holder which could be moved vertically along the cell's tube by a magnet. Before initiating the FTIR measurements, the disk was treated under dynamic vacuum ( $6 \times 10^{-4}$  Torr) at 150 °C for 3 h to remove surface contaminants. After the disk cooling to RT, 10  $\mu\text{L}$  of pyridine was spiked into the cell with a syringe via the septum. After the adsorption-desorption equilibrium, the FTIR spectra of the sample were collected. The physisorbed furfuryl alcohol and pyridine were removed by a further evacuation at 150 °C for 3 min under  $6 \times 10^{-4}$  Torr, and then, another FTIR spectrum of the sample was then taken. The X-ray absorption fine structure data on the Ti K-edge of the sample were recorded at room temperature in transmission mode using ion chambers at beam line BL14W of the Shanghai Synchrotron Radiation Facility (SSRF), China. The station was operated with a Si (111) double crystal monochromator. During the measurement, the synchrotron was operated at energy of 3.5 GeV and a current between 150 and 210 mA. The photon energy was calibrated with the first inflection point of Ti K-edge of Ti metal foil.

### 2.4. Electrochemistry measurement

The working electrode was prepared on fluorine-doped tin oxide (FTO) glass, which was cleaned by sonication in water for 30 min. The FTO slide was dip coated with 10  $\mu\text{L}$  of slurry. The slurry was obtained from mixture of 5 mg powder and 0.5 mL pure water with sonication for 2 h. After air drying naturally, a copper wire was connected to the side part of the FTO glass using a conductive tape. The uncoated parts of the electrode were isolated with an epoxy resin and the exposed area of the electrode was 0.25  $\text{cm}^2$ . The electrochemical measurements were performed in a conventional three electrode cell, using a Pt plate and a saturated Ag/AgCl electrode as counter electrode and reference electrode, respectively. The working electrode was immersed in a 0.2 M  $\text{Na}_2\text{SO}_4$  aqueous solution without any additive for 30 s before measurement. The electrochemical impedance spectroscopy (EIS) was performed at a Zahner electrochemical workstation. The photocurrent measurements were conducted on a Precision PARC workstation. The Mott-Schottky plots were obtained at three different frequencies (0.5 k, 1 k and 1.5 kHz).

### 2.5. Temperature-programmed desorption of ammonia measurement

The temperature-programmed desorption of ammonia was carried out on a Micromeritics Auto Chem 2920 instrument. About 50 mg of a sample was first pretreated at 180 °C for 1 h in a quartz tube, then the sample was cooled to 50 °C to allow for the adsorption of ammonium (3.0%  $\text{NH}_3$  in  $\text{N}_2$ , 30 mL/min) for 1 h. The desorption of ammonium was conducted from 50 to 300 °C at a heating rate of 10 °C/min in a helium flow (40 mL/min), and the desorption amount was monitored by a thermal conductivity detector (TCD).

## 2.6. Evaluation of photocatalytic activity

The photocatalytic oxidation of FA experiments was carried out in a Pyrex reaction tube. A mixture of furfuryl alcohol (0.1 mmol), the as-prepared catalyst (16 mg) was suspended with the solvent of benzotrifluoride (BTF, 1.5 mL) in a 10 mL Pyrex glass bottle. This mixture was saturated with pure oxygen at a pressure of 1 bar and stirred to make the catalyst blend evenly in the solution. After the adsorption-desorption equilibrium, the suspension was irradiated by a 300 W Xe arc lamp with a 420 nm-Cut filter (PLS-SXE 300, Beijing Perfectlight Co. Ltd.). After the 6 h irradiations, the mixture was centrifuged to completely remove the catalyst particles. The remaining solution was determined with an Agilent online gas chromatography (GC 7890, FID). HP-5 column (length, 30 m; inner diameter, 320  $\mu\text{m}$ ; film thickness, 0.25  $\mu\text{m}$ ) was applied for separation of product. Helium (purity 99.999%) was used as the carrier gas at the constant flow rate of 20  $\text{mL min}^{-1}$ . The temperatures of the injector and detector were maintained at 250 and 300  $^\circ\text{C}$ , respectively. The pressure of injection was set at 8.363 psi. Column temperature program was programmed from 50  $^\circ\text{C}$  to 110  $^\circ\text{C}$  at 6  $^\circ\text{C}/\text{min}$ . The injection volume was 1  $\mu\text{L}$ .

$$\text{Conversion (\%)} = \frac{[(\text{C}_0 - \text{C}_{\text{alcohol}})/\text{C}_0] \times 100}{\text{Selectivity (\%)} = [\text{C}_{\text{aldehyde}}/(\text{C}_0 - \text{C}_{\text{alcohol}})] \times 100}$$

$$\text{Where } \text{C}_0 \text{ is the initial concentration of alcohol.}$$

## 3. Results and discussion

As shown in Fig. 1, the X-ray diffraction patterns suggest that the SSR and LAT with a single phase have been prepared successfully [21]. After the proton-exchange process, the diffraction peak (020) shifts towards the lower 20 degree. This indicates that the interlayer distance is expanded from 0.85 nm for SSR to 0.90 nm for LAT according to the Bragg equation. The interlayer  $\text{Cs}^+$  in the original layered counterpart have been replaced with protons in the forms of  $\text{H}_3\text{O}^+$ . This is beneficial to the subsequent cations exchange process for the formation of NST. The diffraction peaks for NST become very weak and broad after the exfoliation process, suggesting the disappearance of the periodic layered structure of  $\text{H}_{1.4}\text{Ti}_{1.65}\text{O}_4\cdot\text{H}_2\text{O}$ . This is an evidence to indicate that the as-prepared sample is sheet-like structure [8,21,22].

SEM images show the samples SSR and LAT with a typical layered structure (Fig. 2A, B). The sample NST exhibits loose and regular ultrathin 2D nanosheet morphology (Fig. 2C). According to the results of Nitrogen adsorption-desorption isotherms, the BET specific surface area of NST is about 183.2  $\text{m}^2/\text{g}$ , which is about 22.3 times larger than that of LAT (8.2  $\text{m}^2/\text{g}$ , Fig. S2). This indicates that the exfoliated  $\text{H}_{1.4}\text{Ti}_{1.65}\text{O}_4\cdot\text{H}_2\text{O}$  maintains the self-governed nanosheet form. After the

exfoliation process, the layered structure of LAT disappears and the NST is obtained. A Tyndall effect is observed in NST suspension (Fig. 3A). Due to the ultrathin thickness of NST, the morphology of NST is nearly transparent in TEM image. The SAED shows the typical single crystal diffraction (Fig. 3B). In addition, the other nanosheets were also selected to confirm the synthesis of the ultrathin nanosheet. Similar with Fig. 3A-D also shows the transparent nanosheet like structure of NST with the single crystal. In addition, the thickness of the nanosheet is determined by AFM (Fig. 4). Result suggests that the average thickness of NST is about 1.2 nm, which could be considered as a monolayer thickness [23].

The as-prepared photocatalyst was used in the oxidation of furfuryl alcohol to fufuraldehyde under visible light irradiation at 25  $^\circ\text{C}$  with oxygen atmosphere using benzotrifluoride as the solvent. The conversions of furfuryl alcohol over the samples are increased with prolonging the visible light irradiation time. After 6 h visible light irradiation, the high conversion of furfuryl alcohol (54%) with the high selectivity of fufuraldehyde (99%) is achieved over the NST (Table 1, entry 3), which is 10 times higher than that of its layered counterpart (Table 1, entry 5). Furthermore, no fufuraldehyde is detected in the absence of a catalyst (Table 1, entry 6). Low conversion of furfuryl alcohol is obtained in the dark condition or under the nitrogen atmosphere, suggesting that the oxidation of furfuryl alcohol is driven by visible light and  $\text{O}_2$  molecules (Table 1, entries 7, 8). The reusability of the photocatalyst has been also tested by three successive recycles (Fig. S3), NST still maintains the high activities. Additionally, no obvious changes have been observed in the XRD patterns (Fig. S4) of fresh and used NST, demonstrating the high stability of the photocatalyst.

The kinetics experiments of the relation between time and FA conversion have been also carried out to explore the optimum reaction time. As shown in Fig. S5A, the conversion of FA and the selectivity of fufuraldehyd were obtained based on the increased reaction time from 1 h to 14 h. It is clear that the conversion of FA shows the linear growth from 0 to 54% with the increase of reaction time during the 6 h visible light irradiation. Simultaneously, the selectivity of fufuraldehyd is also keeping in the value of 99%. After the 6 h, the conversion of FA to fufuraldehyd reached the reaction equilibrium. Prolonging the reaction time to 14 h, the conversion of FA maintains about 54% without any increase. The selectivity of fufuraldehyd shows a slight decrease (93%) due to the over oxidation of FA. Therefore, the 6 h of reaction time is optimal for the aerobic oxidation of FA to fufuraldehyd. Moreover, we studied the kinetic process with the NST, containing the influence of the first 6 h reaction time on the reaction rate for the aerobic oxidation of FA (Fig. S5). The plot of the natural logarithm of the concentration of FA against reaction time gives a straight line, indicating a feature of first-order reaction, with the rate constant obtained from the slope of the line. Thus, the reaction rate for the aerobic oxidation of FA is

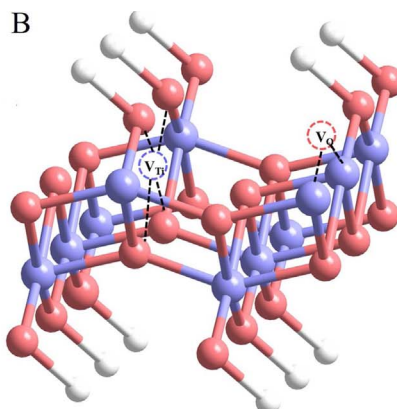
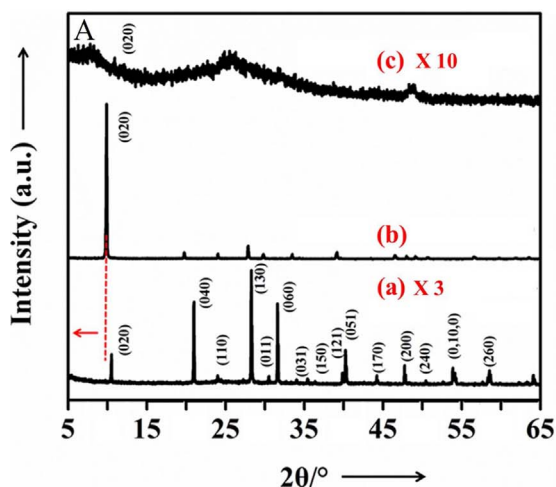


**Fig. 1.** (A) XRD patterns of (a)  $\text{Cs}_{0.7}\text{Ti}_{1.65}\text{Zn}_{0.35}\text{O}_4$ , (b) layered  $\text{H}_{1.4}\text{Ti}_{1.65}\text{O}_4\cdot\text{H}_2\text{O}$  and (c)  $\text{H}_{1.4}\text{Ti}_{1.65}\text{O}_4\cdot\text{H}_2\text{O}$  nanosheet; (B) Schematic structure of  $\text{H}_{1.4}\text{Ti}_{1.65}\text{O}_4\cdot\text{H}_2\text{O}$  nanosheet, Atoms are color labeled: Ti (blue), H (white), and O (red). (For interpretation of the references to colour in this figure legend, the reader is referred to the web version of this article.)

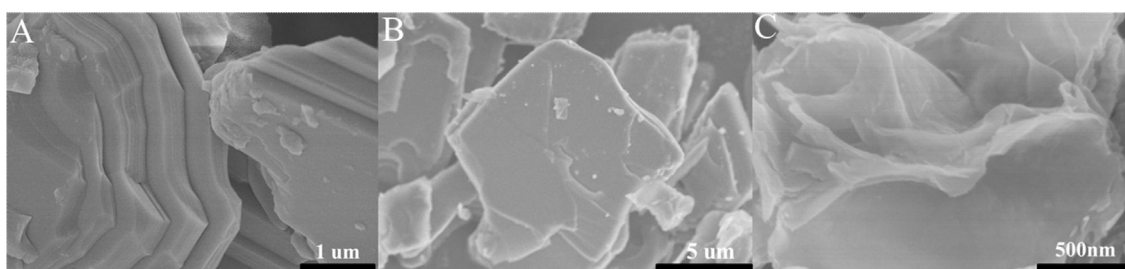


**Fig. 2.** SEM images of (A)  $\text{Cs}_{0.7}\text{Ti}_{1.65}\text{Zn}_{0.35}\text{O}_4$ , (B) layered  $\text{H}_{1.4}\text{Ti}_{1.65}\text{O}_4\cdot\text{H}_2\text{O}$  and (C)  $\text{H}_{1.4}\text{Ti}_{1.65}\text{O}_4\cdot\text{H}_2\text{O}$  nanosheet.

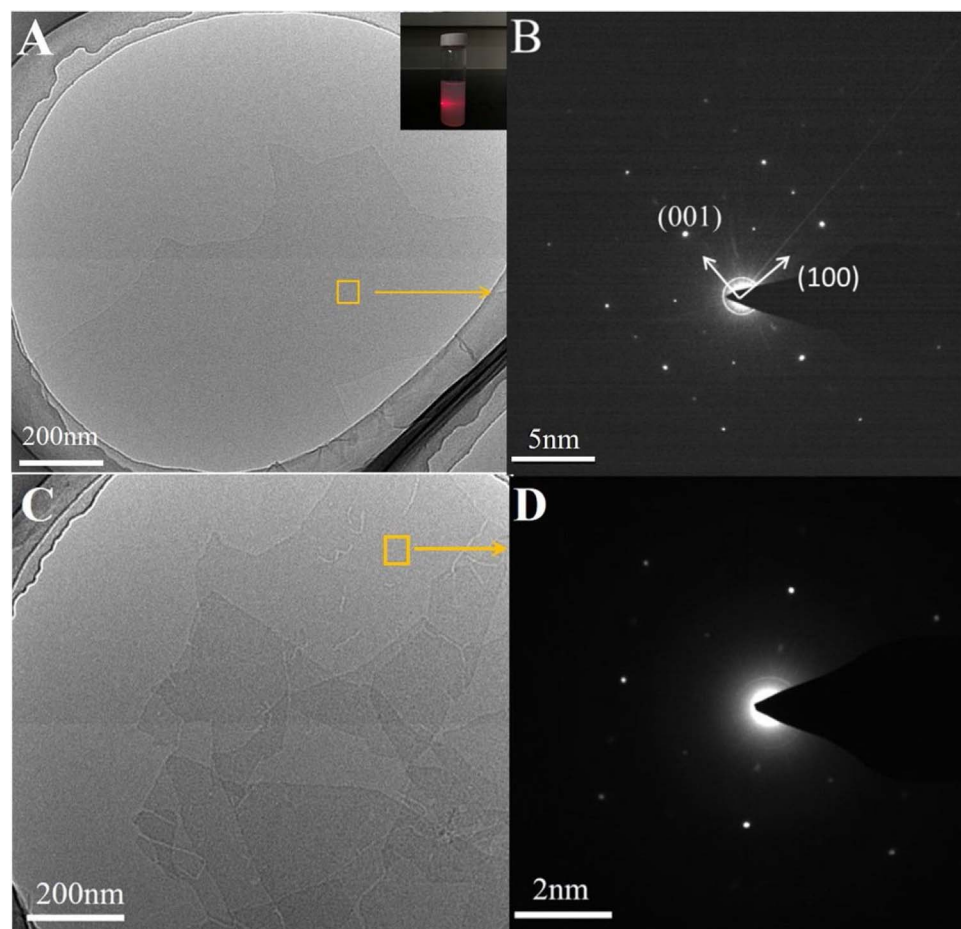


**Fig. 3.** (A, C) TEM images of  $\text{H}_{1.4}\text{Ti}_{1.65}\text{O}_4\cdot\text{H}_2\text{O}$  nanosheet; (B, D) the corresponding SAED of  $\text{H}_{1.4}\text{Ti}_{1.65}\text{O}_4\cdot\text{H}_2\text{O}$  nanosheet colloidal suspension.

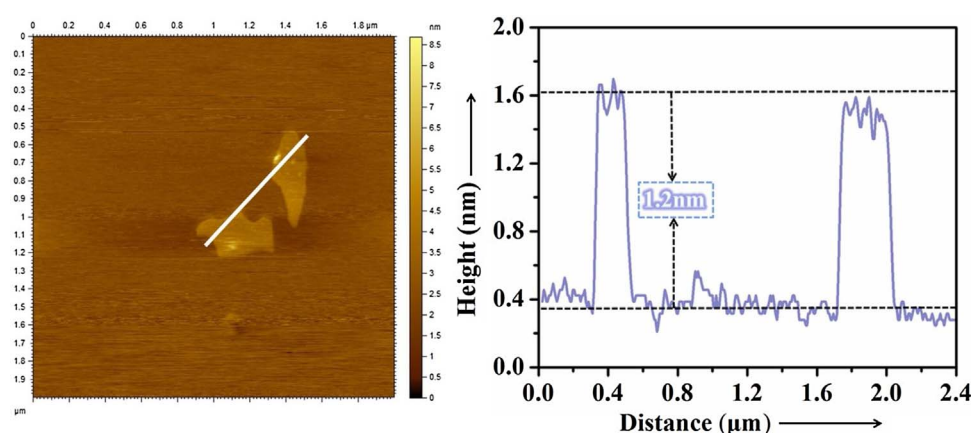


**Fig. 4.** AFM images of  $\text{H}_{1.4}\text{Ti}_{1.65}\text{O}_4\cdot\text{H}_2\text{O}$  nanosheet.

**Table 1**

Photocatalytic activity for the oxidation of furfuryl alcohol over NST with visible light irradiation<sup>a</sup>.

Entry	Catalyst	Time (h)	$h\nu^b$	Atmosphere	Conv. (%)	Sel. (%)
1	NST	2	+	O <sub>2</sub>	16.7	99
2	NST	4	+	O <sub>2</sub>	35.6	99
3	NST	6	+	O <sub>2</sub>	54.0	99
4	LAT	4	+	O <sub>2</sub>	2.1	99
5	LAT	6	+	O <sub>2</sub>	5.8	99
6	—	6	+	O <sub>2</sub>	—	—
7	NST	6	—	O <sub>2</sub>	3.1	99
8	NST	6	+	N <sub>2</sub>	4.6	99

<sup>a</sup> Reaction condition: furfuryl alcohol (0.1 mmol), catalyst (16 mg), benzotrifluoride (1.5 mL), O<sub>2</sub> (1 atm), irradiation time (6 h).

<sup>b</sup>  $\lambda \geq 420$  nm. NST: H<sub>1.4</sub>Ti<sub>1.65</sub>O<sub>4</sub>H<sub>2</sub>O nanosheet, LAT: layered H<sub>1.4</sub>Ti<sub>1.65</sub>O<sub>4</sub>H<sub>2</sub>O.

0.137 h<sup>-1</sup> in the first reaction of 6 h according to Fig. S5B.

To investigate the influence of solvent effect on the selectivity of furfuraldehyde. A series of solvents such as water, acetonitrile, Toluene, and dimethyl sulfoxide were also selected for the oxidation of FA, respectively (Table S1). It can be observed that the NST shows the highest transformation efficiency towards FA (95.9%) with acetonitrile as the solvent. However, the selectivity of furfuraldehyde was only 32.3%. Only the 17.3% conversion of FA and the 3.2% selectivity of furfuraldehyde was obtained using the dimethyl sulfoxide (DMSO) as solvent. It should be noted that the order of the selectivity of furfuraldehyde in different solvent greatly depends on the polar of solvent. The order of the selectivity of furfuraldehyde in different solvent is the follow: Benzotrifluoride > Toluene > Acetonitrile > Water > DMSO. However, the selectivity of furfuraldehyde is decreased with the increased polar of solvent (DMSO > Water > Acetonitrile > Toluene > Benzotrifluoride). In addition, the benzotrifluoride shows the better property of the dissolved oxygen than water and acetonitrile. Considering that the photocatalytic selective oxidation of alcohols is an aerobic reaction. Thus, the benzotrifluoride was selected as the suitable solvent for the oxidation of FA at oxygen atmosphere.

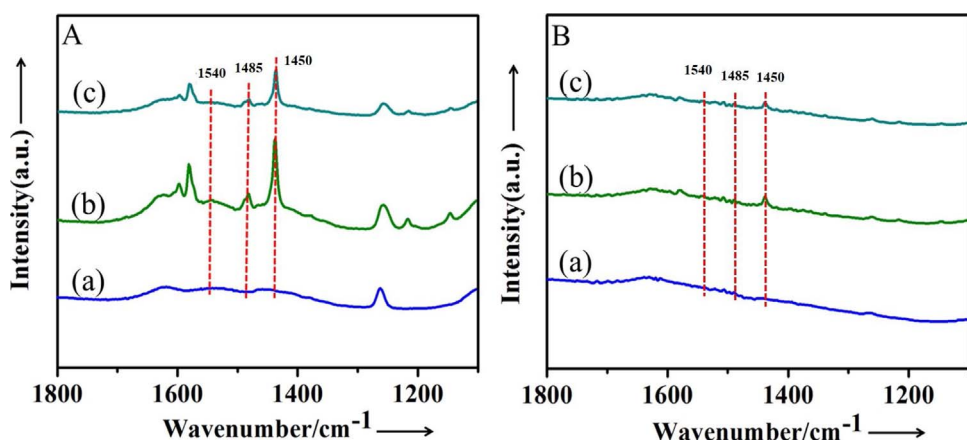
The electrochemical analyses were carried out to explore the transfer and separation efficiency of photo-generated electrons and holes. Fig. S6A displays the photocurrent transient response of NST and LAT under intermittent light irradiation. An enhanced photocurrent density of NST is clearly observed, suggesting the efficient separation of photogenerated electron-hole pairs in NST. This is in good agreement with the photoluminescence (PL) results (Fig. S6B). Meanwhile, the electrochemical impedance spectra (EIS) for the samples exhibit that

NST has the smaller arc as compared to the LAT (Fig. S7), meaning that NST has higher efficiency of surface charge transfer. Therefore, the higher charge mobility and separation efficiency on NST may be one of reasons for improving photocatalytic activity.

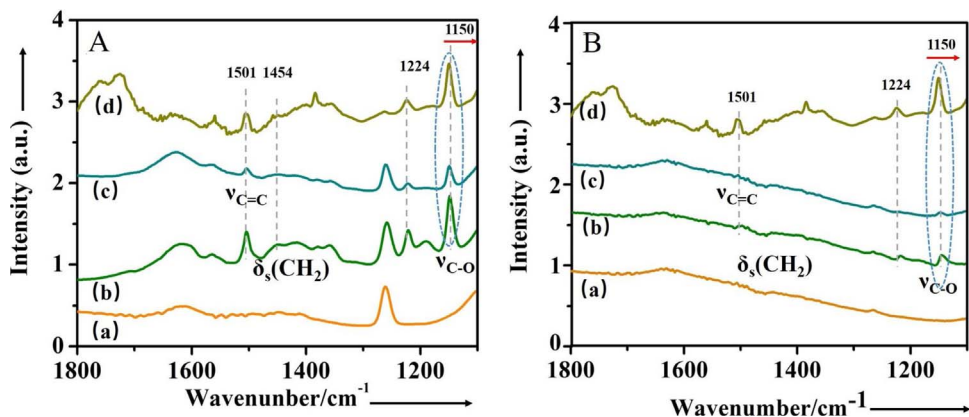
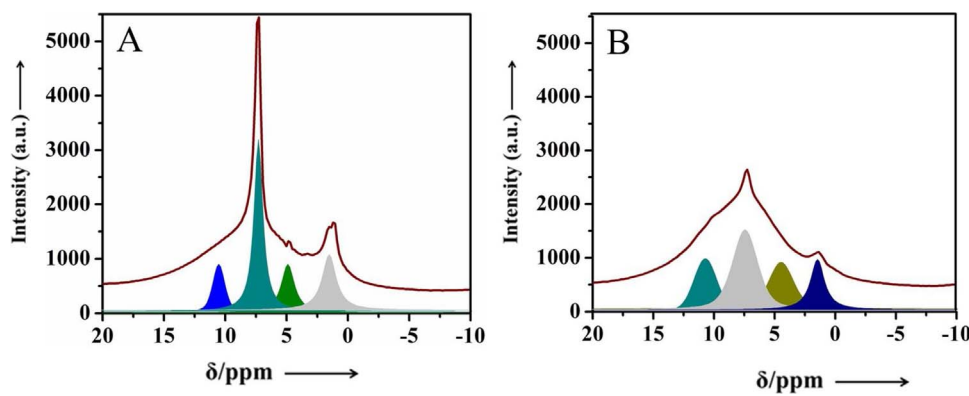
Previous studies reported that the oxidation of alcohols could be promoted by the superficial Lewis and Brønsted acid sites for photocatalysts [8,24]. Therefore, the superficial acidity and acid species in photocatalysts have been investigated by in-situ FTIR and <sup>1</sup>H NMR. Fig. 5A shows the in-situ FTIR of pyridine absorption on NST, a strong peak at 1450 cm<sup>-1</sup> is observed, suggesting the pyridine molecules on the Lewis acid sites. Besides, there are also two broad and weak peaks at 1540 cm<sup>-1</sup> and 1485 cm<sup>-1</sup>, indicating that pyridine molecules on the Brønsted acid sites in NST [9b]. These peaks still exist even after evacuation indicating the chemisorption of pyridine on the surface of NST. As a comparison, the layered sample exhibits much weaker intensities of peaks (Fig. 5B). These results suggest that the NST has more surface Lewis and Brønsted acid sites than the layered counterpart. Brønsted acids can greatly enhance the conversion rate of alcohols, and Lewis acidic sites may be considered as the active sites. Therefore, the strong Brønsted and Lewis acidity would promote the catalytic transformation efficiency of FA.

Fig. 6 shows <sup>1</sup>H NMR spectra of LAT and NST after the removal of adsorbed water. For NST, there are four peaks at 10.72, 7.32, 4.84 and 1.37 ppm ascribed to OH groups, Ti (OH) Ti, hydrogen-bonded Ti-OH, and isolated Ti-OH, respectively [25]. The bridging hydroxyl groups, Ti (OH) Ti, may be considered as a Brønsted acid site [26]. Notably, the intensity of the bridging hydroxyl in NST is higher than that in LAT (Fig. 6B), indicating the stronger acidity in NST. The NH<sub>3</sub>-TPD experiments for NST and LAT were also carried out to further study the difference in amount of the acid site between NST and LAT. As shown in Fig. S8. There are two strong peaks at 98 and 250 °C for the NST, which can be attributed to the physisorption and chemisorption of NH<sub>3</sub> on the surface acid sites, respectively. However, no obvious peaks of NH<sub>3</sub> were observed for LAT, suggesting that the much less acid sites on LAT are exposed than those on NST. Moreover, the distinct morphology would provide a more open structure for the exposure of acid sites and absorption of NH<sub>3</sub> compared with the compact structure of LAT. Thus, the NST shows the high ability for the absorption of NH<sub>3</sub> and pyridine (Fig. 5). That is in well agreement with in-situ FT-IR results of pyridine adsorption.

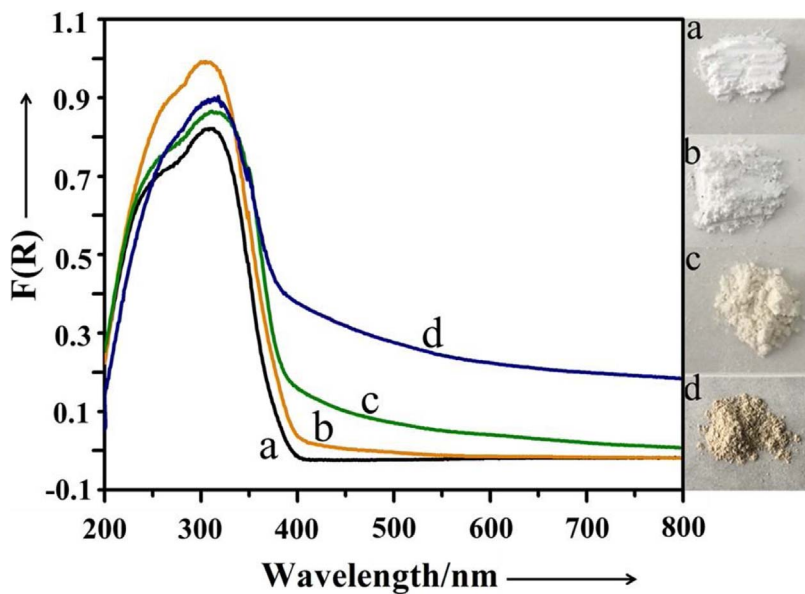
The interactions between the catalysts and the FA molecules have been revealed by in-situ FTIR of FA absorption. As shown in Fig. 7, the FA molecules are chemisorbed and physisorbed on the surface of NST (Fig. 7A). There are three peaks are witnessed about 1501 cm<sup>-1</sup>, 1454 cm<sup>-1</sup> and 1150 cm<sup>-1</sup> assigned to the ring of C=C stretching vibration, CH<sub>2</sub> scissor bending vibration and the C–O bond stretching vibration peak, respectively [8,10][8,10b]. However, the weaker peaks are observed on LAT, suggesting that the LAT has the poor adsorption to



**Fig. 5.** In situ FT-IR spectra of H<sub>1.4</sub>Ti<sub>1.65</sub>O<sub>4</sub>H<sub>2</sub>O nanosheet (A) and layered H<sub>1.4</sub>Ti<sub>1.65</sub>O<sub>4</sub>H<sub>2</sub>O (B) adsorbed pyridine. (a) Disk degassed at 150 °C for 3 h. (b) Adsorption for 30 min at RT (physisorption + chemisorption). (c) A further evacuation of excess furfuryl alcohol at  $6 \times 10^{-4}$  Torr for 3 min after adsorbed furfuryl alcohol 30 min (chemisorption).



**Fig. 7.** In situ FT-IR spectra of  $\text{H}_{1.4}\text{Ti}_{1.65}\text{O}_4\text{H}_2\text{O}$  nanosheet (A) and layered  $\text{H}_{1.4}\text{Ti}_{1.65}\text{O}_4\text{H}_2\text{O}$  (B) adsorbed furfuryl alcohol. (a) Disk degassed at 150 °C for 3 h. (b) Adsorption for 30 min at RT (physisorption + chemisorption). (c) A further evacuation of excess furfuryl alcohol at  $6 \times 10^{-4}$  Torr for 3 min after adsorbed furfuryl alcohol 30 min (chemisorption). (d) FT-IR spectra of furfuryl alcohol.



FA than the NST. Additionally, the peak at  $1150\text{ cm}^{-1}$  can be assigned to the  $\nu_{\text{C}-\text{O}}$  in absorbed FA molecules (Fig. 7). The peak is shifted to the lower wavenumber compared with that in free FA molecules. This may indicate that FA can efficiently chemisorb in the Lewis acid sites via C–O groups. Due to the exposed Lewis acid sites in catalyst, the surface C–O...Ti coordination species would be formed. The in situ FTIR for furfuraldehyde absorption (Fig. S9) was also carried out to reveal the interaction between the NST and furfuraldehyde, because desorption of the formed furfuraldehyde from the NST is crucial for the inhibition of over oxidation. As shown in Fig. S9, there is an obvious peak at  $1684\text{ cm}^{-1}$  assigned to the  $\sigma(\text{C}=\text{O})$  of furfuraldehyde [27]. However, the peak of

$\sigma(\text{C}=\text{O})$  disappears after the further evacuation, suggesting that the furfuraldehyde could easily desorb from the NST. This facilitates the cycle absorption of FA and the high selectivity of furfuraldehyde over the NST.

The influence of these coordination species on catalysts and FA molecules have been further studied by UV-DRS. Fig. 8 suggests that the naked LAT and NST with white color can only absorb the UV light ( $\lambda < 350\text{ nm}$ ). When the FA absorbed, both NST and LAT exhibit a visible light absorption property. Considering that FA molecules could not absorb the visible light (Fig. S10), these may be due to a strong acid-base interaction between furfuryl alcohol and NST through the

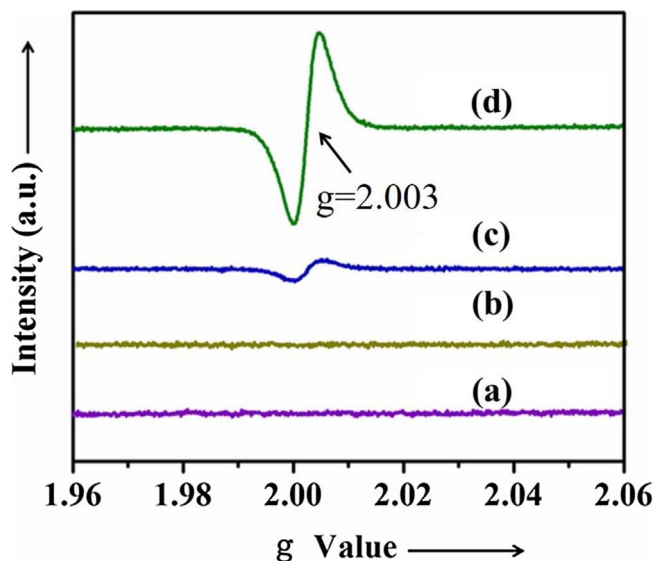


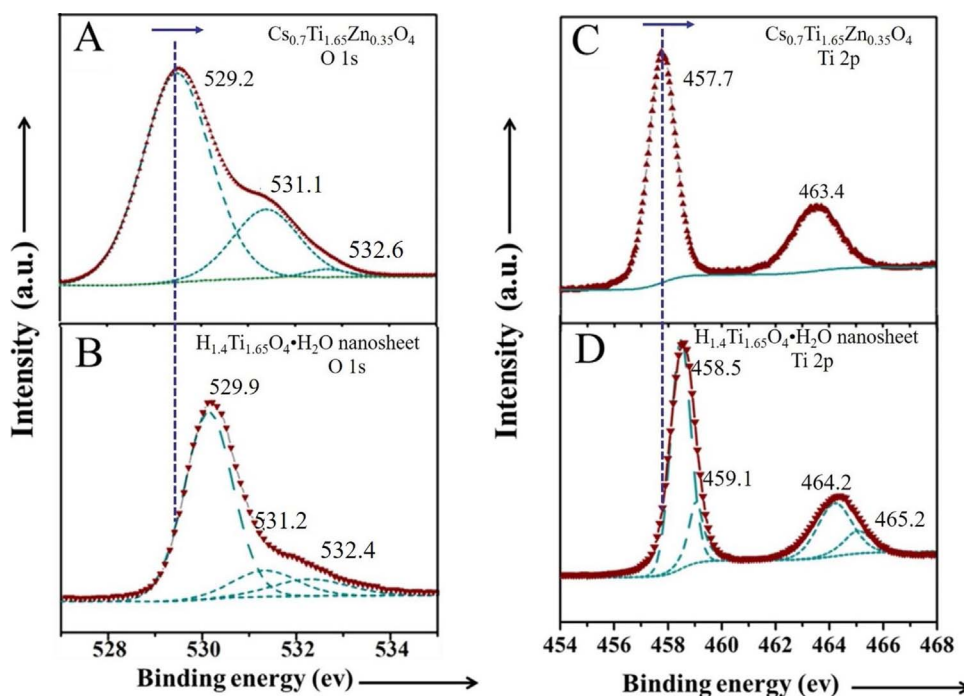
**Fig. 9.** In-situ EPR spectra of the samples, (a) layered  $\text{H}_{1.4}\text{Ti}_{1.65}\text{O}_4\cdot\text{H}_2\text{O}$  with visible light, (b)  $\text{H}_{1.4}\text{Ti}_{1.65}\text{O}_4\cdot\text{H}_2\text{O}$  nanosheet with visible light, (c) furfuryl alcohol/layered  $\text{H}_{1.4}\text{Ti}_{1.65}\text{O}_4\cdot\text{H}_2\text{O}$  with visible light, (d) furfuryl alcohol/ $\text{H}_{1.4}\text{Ti}_{1.65}\text{O}_4\cdot\text{H}_2\text{O}$  nanosheet with visible light.

formation of a surface coordination species. These suggest that the surface coordination species can induct the surface charge transfer from “Ligand to metal”, resulting the expanded visible light absorption of catalyst. However, the dark yellow FA/NST show enhanced photo-absorption intensity compared with the light yellow FA/LAT because of the higher concentration of surface coordination species in NST. These results are consistent with the in-suit FTIR. Notably, a weak photo-absorption for NST in the range of 400–550 nm has also been observed. This may be caused by the defects [28,29].

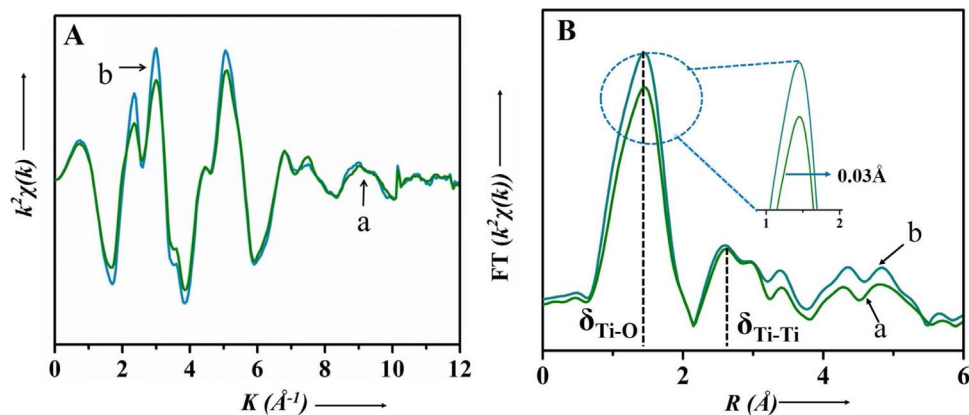
The variations in the microstructure of catalysts with FA adsorbed have been investigated by ESR. The ESR signal at  $g = 2.003$  is observed over the FA/NST sample under visible light irradiation (Fig. 9), assigning to the oxygen vacancy [30,31]. At the same conditions, a much weaker signal intensity of oxygen vacancy can be seen in FA/LAT

sample. However, the naked NST and LAT show no signals under visible light irradiation, indicating that the absorption of FA molecules can result in the producing of oxygen vacancy in catalysts. Due to the formation of surface coordination species between FA molecules and surface Lewis acid sites via the C–O groups, the nearby oxygen atom of Ti atoms (Lewis acid sites) would bond with the O–H groups via hydrogen bonds. Thus, the binding of Ti–O in catalysts would be weakened forming oxygen vacancies. Because of the more exposed Lewis acid sites and oxygen atoms around them in the NST than those in the LAT, higher concentration of oxygen vacancy on the surface of FA/NST is observed.

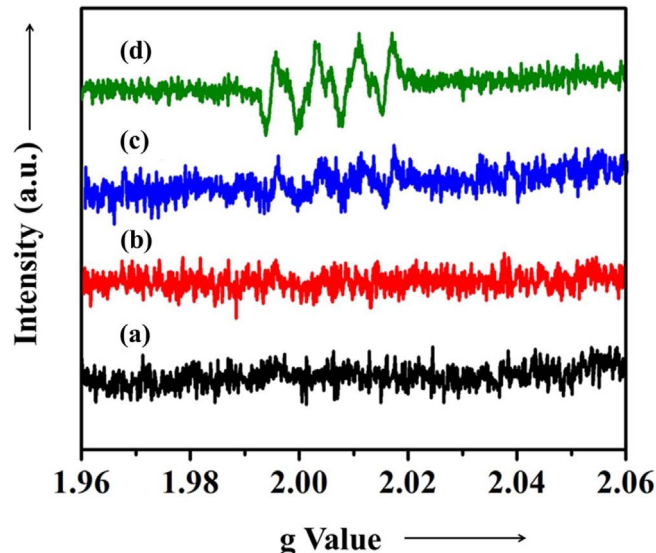
To further understand the effect of the microstructure of NST on the surface coordination species, the XPS and XAFS measurements have been further performed. Fig. 10 exhibits the XPS analysis of Ti 2p and O 1s. The O 1s spectrum for SSR could be fitted into three peaks at 529.2, 531.1 and 532.6 eV (Fig. 10A) corresponding to signals of 2-coordinated oxygen O1, 4-coordinated oxygen O2 and the adsorbed oxygen species respectively [21,32]. Notably, the enhanced binding energy of O1 in NST suggests the weak bond of O1 with interlayer ions via the acid exchange (Fig. 10B). However, the binding energy of O2 components is not changed. The XPS for the FA-absorbed NST sample was characterized to further investigate the chemical state of surface oxygen atoms. As shown in Fig. S11B, the curve of O 1s in FA/NST shows the slightly different shape with the pure NST after the absorption of FA. The spectrum of O1s can be also fitted into three peaks at 529.9, 531.2, and 532.4. The peaks at 529.9 and 531.2 can be assigned to the lattice O1, O2 and absorbed oxygen in FA/NST respectively [21]. The positions of binding energy for O1 and O2 show no obvious changes before and after the absorption of FA (Fig. S11). The peak of adsorbed oxygen species shifts to a lower value of binding energy from 532.4 eV in FA/NST to 532.2 eV in NST due to the introduction of alcohol hydroxyl group in FA. It should be noted that the adsorption of FA could theoretically introduce a new hydroxyl species peak in the spectrum of O1s at the 531.9 eV. However, none peak can be fitted at position of 531.9 eV in the spectrum of O1s. Thus, we can deduce that the adsorption of FA on the NST may result in the charge transfer from FA to the NST via the formed surface coordination species. The electron cloud density of O atoms in the alcohol hydroxyl group of FA would be decreased and the position of O1s for the alcohol hydroxyl group may



**Fig. 10.** O 1s XPS spectra of (A)  $\text{Cs}_{0.7}\text{Ti}_{1.65}\text{Zn}_{0.35}\text{O}_4$  and (B)  $\text{H}_{1.4}\text{Ti}_{1.65}\text{O}_4\cdot\text{H}_2\text{O}$  nanosheet, Ti 2p XPS spectra of (C)  $\text{Cs}_{0.7}\text{Ti}_{1.65}\text{Zn}_{0.35}\text{O}_4$  and (D)  $\text{H}_{1.4}\text{Ti}_{1.65}\text{O}_4\cdot\text{H}_2\text{O}$  nanosheet.

**Table 2**Structural parameters around Ti atoms in  $\text{TiO}_2$ , layered  $\text{H}_{1.4}\text{Ti}_{1.65}\text{O}_4\text{H}_2\text{O}$  and  $\text{H}_{1.4}\text{Ti}_{1.65}\text{O}_4\text{H}_2\text{O}$  nanosheet extracted from EXAFS curve-fitting.

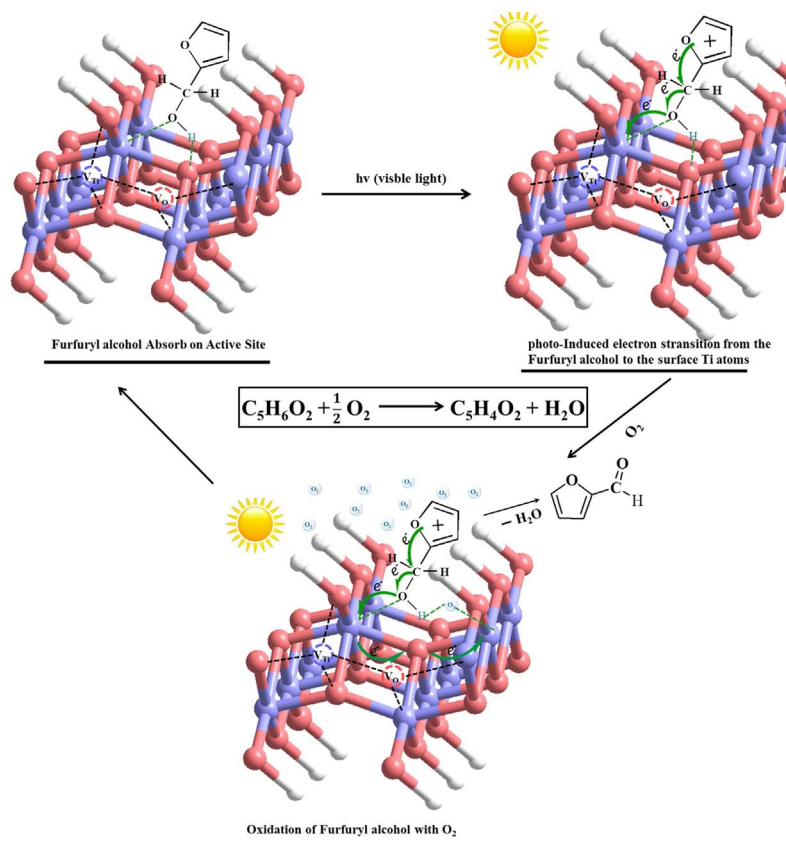
sample	path	N	$R(\text{\AA})$	$\delta^2(10^{-3} \text{\AA})$	$\Delta E_0(\text{ev})$
$\text{TiO}_2$ (anatase)	Ti-O1	2.0	$1.894 \pm 0.01$	$3.3 \pm 0.001$	$-0.48 \pm 0.1$
	Ti-O2	4.0	$1.972 \pm 0.01$	$3.3 \pm 0.001$	$-0.48 \pm 0.1$
	Ti-Ti1	4.0	$3.036 \pm 0.012$	$3.9 \pm 0.001$	$-5.05 \pm 1.4$
	Ti-Ti2	4.0	$3.782 \pm 0.014$	$3.9 \pm 0.001$	$-5.05 \pm 1.4$
LAT	Ti-O1	$2.3 \pm 0.3$	$1.837 \pm 0.02$	$4.7 \pm 0.002$	$-0.75 \pm 1.0$
	Ti-O2	$3.7 \pm 0.6$	$1.976 \pm 0.02$	$4.7 \pm 0.002$	$-0.75 \pm 1.0$
	Ti-Ti1	$3.2 \pm 0.6$	$3.036 \pm 0.01$	$7.3 \pm 0.002$	$-1.88 \pm 2.0$
	Ti-Ti2	$2.8 \pm 0.5$	$3.220 \pm 0.01$	$7.3 \pm 0.002$	$-1.88 \pm 2.0$
NST	Ti-O1	$1.9 \pm 0.3$	$1.828 \pm 0.001$	$3.4 \pm 0.001$	$-1.34 \pm 2.0$
	Ti-O2	$3.0 \pm 0.5$	$1.967 \pm 0.001$	$3.4 \pm 0.001$	$-1.34 \pm 2.0$
	Ti-Ti1	$3.1 \pm 0.6$	$3.046 \pm 0.002$	$8.7 \pm 0.002$	$-0.63 \pm 2.0$
	Ti-Ti2	$2.8 \pm 0.5$	$3.230 \pm 0.002$	$8.7 \pm 0.002$	$-0.63 \pm 2.0$

Fig. 12. 5,5-dimethyl-1-pyrroline-N-oxide trapping ESR spectra of the samples, (a) layered  $\text{H}_{1.4}\text{Ti}_{1.65}\text{O}_4\text{H}_2\text{O}$  with visible light, (b)  $\text{H}_{1.4}\text{Ti}_{1.65}\text{O}_4\text{H}_2\text{O}$  nanosheet with visible light, (c) 5,5-dimethyl-1-pyrroline-N-oxide/layered  $\text{H}_{1.4}\text{Ti}_{1.65}\text{O}_4\text{H}_2\text{O}$  with visible light, (d) 5,5-dimethyl-1-pyrroline-N-oxide/ $\text{H}_{1.4}\text{Ti}_{1.65}\text{O}_4\text{H}_2\text{O}$  nanosheet with visible light.

shift to a higher value of binding energy. These phenomena could further validate the results of in situ FTIR for FA adsorption and UV-DRS. Fig. 10C shows the Ti 2p curve with a high symmetrical profile, suggesting a single chemical state of the Ti atoms in the catalysts. The binding energy value of Ti 2p<sub>3/2</sub> in NST shift from 457.7 to 458.5 eV compared with that in SSR (Fig. 10D), suggesting that the interactions between the Ti atoms and coordinated oxygen atoms are enhanced after the protonic exchange and exfoliation process. The coordination

environments of Ti are further investigated by extended XAFS. As shown in Fig. 11A, the Ti K-edge XAFS  $k^2\chi(k)$  oscillation curve for NST is a similar with that of LAT in frequency but remarkable droop in amplitude. As shown in Fig. 11B, it can be more distinctly demonstrated by the Fourier transform (FT) of the  $k^2\chi(k)$  functions in R-space. The curve is divided into two main peaks at 1.0 \AA and 2.5 \AA associated with the first Ti–O shell and Ti–Ti shell, respectively [33–37]. The intensities of Ti–O and Ti–Ti coordination in NST are dropped significantly compared with those in LAT. These may indicate the reduced coordination numbers and the change of disorder in NST. Furthermore, the peak position of Ti–O is shifted from 1.44 to 1.47 \AA in the higher R direction after exfoliated LAT to NST. It is suggested that the interatomic distances of all the Ti–O coordination in the NST were slightly elongated and their angle of disorder was greatly increased as comparison with the counterpart. A least-squares curve fitting was accomplished to obtain quantitative structural parameters around Ti atoms restricted in LAT and NST (Table 2). As for the NST, both the distances and coordination numbers for Ti–O1, Ti–O2, Ti–Ti1 coordinations showed an obvious decrease as compared with the bulk counterpart. These indicate that the loss of the neighboring O atom in the adjacent layer did not render an obvious change of the monolayer structure, but resulted in a slight structural distortion and the formation of oxygen vacancies. Furthermore, the Debye–Waller factor of the Ti–Ti shell for NST ( $0.0087 \text{\AA}^2$ ) is distinctly larger than that of the layered counterpart ( $0.0073 \text{\AA}^2$ ), further suggesting a distorted octahedral Ti–O environment in NST (Table 2) [38,39]. Therefore, the structural distortion for NST would provide an open structure to expose the active sites efficiently.

In-situ ESR spectra are used to track the roles of  $\text{O}_2$  molecules in photocatalysis. None NST or LAT show the ESR signal at air atmosphere under light irradiation. When the 5,5-dimethyl-1-pyrroline-N-oxide added, six strong ESR signal peaks attributed to  $\cdot\text{O}_2^-$  are observed (Fig. 12) [40,41]. The  $\cdot\text{O}_2^-$  species may mainly originate from the



**Scheme 1.** Probable reaction mechanism of the photocatalytic oxidation of FA over NST with molecular oxygen.

reduction of adsorbed  $\text{O}_2$  molecules by the photogenerated electrons. Due to the efficient photogenerated electrons-holes separation, the NST shows the greatly enhanced signal intensity of  $\cdot\text{O}_2^-$  species compared with LAT.

Based on the above experimental results, a possible photocatalytic mechanism is proposed to elucidate the photocatalytic oxidation of FA to furfuraldehyde under visible light irradiation. As shown in Scheme 1. FA molecules are adsorbed and activated on the surface Lewis acid sites in NST in the form of the coordination species. Under visible light irradiation, the NST/FA is excited and photogenerated electrons/holes are generated. The conduction band of the NST (CB) is  $-0.58$  eV (Fig. S12), which is more negative than that of the  $\text{O}_2/\cdot\text{O}_2^-$  ( $-0.33$  eV vs. NHE). It is thermodynamically permissible for the  $\text{O}_2$  is trapped by photogenerated electrons to form  $\cdot\text{O}_2^-$  possesses a strong oxidation capacity. The consummation of photogenerated electrons could suppress the recombination of photogenerated electron-hole pairs further enhancing photocatalytic activity. Moreover, the adsorbed FA on NST would be deprotonated, forming active intermediate species ( $\text{C}_5\text{H}_5\text{O}_2^+$ ). The  $\text{C}_5\text{H}_5\text{O}_2^+$  would further release a proton under the assistance of  $\cdot\text{O}_2^-$  to form furfuraldehyde. Finally, the weak interactions between NST and furfuraldehyde make the successful releasing of the produced furfuraldehyde from surface of NST, resulting in the high selectivity of furfuraldehyde. The regeneration of  $\text{Ti}^{4+}$  would be reused to absorb FA molecules achieving the reaction cycles.

#### 4. Conclusion

In summary, we have explored the monolayer NST for the photocatalytic oxidation of furfuryl alcohol to furfuraldehyde under visible light irradiation. Surface unsaturated Ti atoms can serve as Lewis acid sites in the catalyst. The FA molecules could adsorb on the sites of the sample via the C–O groups forming the surface coordination species. The photocatalytic reaction is initiated by the photoexcited surface coordination species. Simultaneously, the photogenerated electrons

would transfer from the surface coordination species to the adsorbed oxygen molecule in nearby sites to form active  $\cdot\text{O}_2^-$ . And then, FA is oxidized by this  $\cdot\text{O}_2^-$  to furfuraldehyde. Due to the disorder and open structure of NST, more surface Lewis acid sites are efficiently exposed. Thus, the photocatalytic activity of NST is much higher than that of the layered sample. This work highlights not only the development of the photocatalyst, but also the deep understanding for the interactions between photocatalysts and reactant molecules.

#### Conflict of interest

The authors declare no competing financial interest.

#### Acknowledgments

This work is supported by the National Natural Science Foundation of China (21677036 and 51672048), the major science and technology projects of Fujian Province (2015YZ0001-1). S. Liang also thanks the Natural Science Funds for Distinguished Young Scholar of Fujian Province (2016J06004). The authors also thank the Shanghai Synchrotron Radiation Facility of China for the XAFS spectra measurements at the < BL14W1 beamline.

#### Appendix A. Supplementary data

Supplementary data associated with this article can be found, in the online version, at <http://dx.doi.org/10.1016/j.apcatb.2017.10.069>.

#### References

- [1] X.J. Lang, X.D. Chen, J.C. Zhao, Chem. Soc. Rev. 43 (2014) 473–486.
- [2] S. Sarina, E. Waclawik, H.Y. Zhu, Green Chem. 15 (2013) 1814–1833.
- [3] J.H. Kou, C.H. Lu, J. Wang, Y. k. Chen, Z.Z. Xu, R. Varma, Chem. Rev. 117 (2017) 1445–1514.
- [4] Y.T. Gong, M.M. Li, H.R. Li, Y. Wang, Green Chem. 17 (2015) 715–736.

[5] O. Tomita, T. Otsubo, M. Higashi, B. Ohtani, R. Abe, *ACS Catal.* 6 (2016) 1134–1144.

[6] Q. Li, X. Li, S. Wageh, A. Al-Ghamdi, J.G. Yu, *Adv. Energy Mater.* 5 (2015) 14.

[7] J. Colmenares, W.Y. Ouyang, M. Ojeda, E. Kuna, O. Chernyayeva, D. Lisovitskiy, S. De, R. Luque, A. Balu, *Appl. Catal. B: Environ.* 183 (2016) 107–112.

[8] S.J. Liang, L.R. Wen, S. Lin, J.H. Bi, P.Y. Feng, X.Z. Fu, L. Wu, *Angew. Chem. Int. Ed.* 126 (2014) 2995–2999.

[9] (a) X.J. Lan, X.D. Chen, J.C. Zhao, *Chem. Soc. Rev.* 43 (2014) 473–486.

[10] (a) X. Yang, H. Zhao, J.F. Feng, Y.N. Chen, S.Y. Gao, R. Cao, *J. Catal.* 351 (2017) 59–66.

[11] M. Zakrzewska, E. Bogel-Łukasik, R. Bogel-Łukasik, *Chem. Rev.* 111 (2011) 397–417.

[12] S. Yurdakal, B.S. Tek, O. Alagoz, V. Augugliaro, V. Loddo, G. Palmisano, L. Palmisano, *ACS Sustain. Chem. Eng.* 1 (2013) 456–461.

[13] B. Zhang, J. Li, Y.Y. Gao, R.F. Chong, Z.L. Wang, L. Guo, X.W. Zhang, C. Li, *J. Catal.* 345 (2017) 96–103.

[14] B.R. Kim, J.S. Oh, J. Kim, C.Y. Lee, *Catal. Lett.* 146 (2016) 734–743.

[15] (a) Z.Q. Sun, T. Liao, Y.H. Dou, S.M. Hwang, M. Park, L. Jiang, J.H. Kim, S.X. Dou, *Nat. Commun.* 5 (2014) 3813.

[16] (a) S.L. Zhang, M.Q. Xie, F.Y. Li, Z. Yan, Y.F. Li, E. Kan, W. Liu, Z.F. Chen, H.B. Zeng, *Angew. Chem. Int. Ed.* 55 (2016) 1666–1669.

[17] Q.Y. Lin, L. Li, S.J. Liang, M.H. Liu, J.H. Bi, L. Wu, *Appl. Catal. B: Environ.* 163 (2015) 135–142.

[18] X.D. Zhang, X. Xie, H. Wang, J.J. Zhang, B.C. Pan, Y. Xie, *J. Am. Chem. Soc.* 135 (2013) 18–21.

[19] M. Kitano, E. Wada, K. Nakajima, S. Hayashi, S. Miyazaki, H. Kobayashi, M. Hara, *Chem. Mater.* 25 (2013) 385–393.

[20] (a) J.F. Xie, S. Li, X.D. Zhang, J.J. Zhang, R.X. Wang, H. Zhang, B.C. Pan, Y. Xie, *Chem. Sci.* 5 (2014) 4615–4620.

[21] T. Gao, H. Fjellvag, P. Norby, *Chem. Mater.* 21 (2009) 3503–3513.

[22] (a) Y. Omomo, T. Sasaki, L. Zhou, M. Watanabe, *J. Am. Chem. Soc.* 125 (2003) 3568–3575.

[23] T. Maluangnont, K. Matsuba, F.X. Geng, R.Z. Ma, Y. Yamauchi, T. Sasaki, *Chem.* Mater. 25 (2013) 3137–3146.

[24] Q. Wang, M. Zhang, C.C. Chen, W.H. Ma, J.C. Zhao, *Angew. Chem.* 122 (2010) 8148.

[25] A. Takagaki, T. Yoshida, D. Lu, J. Kondo, M. Hara, K. Domen, S. Hayashi, *J. Phys. Chem. B* 108 (2004) 11549–11555.

[26] M. Kitano, K. Nakajima, J. Kondo, S. Hayashi, M. Hara, *J. Am. Chem. Soc.* 132 (2010) 6622–6623.

[27] C. Keresszegi, D. Ferri, T. Mallat, A. Baiker, *J. Catal.* 234 (2005) 64–75.

[28] M. Kong, Y.Z. Li, X. Chen, T.T. Tian, P.F. Fang, F. Zheng, X.J. Zhao, *J. Am. Chem. Soc.* 133 (2011) 16414–16417.

[29] X.M. Yu, B. Kim, Y.K. Kim, *ACS Catal.* 3 (2013) 2479–2486.

[30] Z. Wei, Y.F. Liu, J. Wang, R.L. Zong, W.Q. Yao, J. Wang, Y.F. Zhu, *Nanoscale* 7 (2015) 13943–13950.

[31] K. Xu, H. Ding, H.F. Lv, P.Z. Chen, X.L. Lu, H. Cheng, T.P. Zhou, S. Liu, X.J. Wu, C.Z. Wu, Y. Xie, *Adv. Mater.* 28 (2016) 3326–3332.

[32] C. Perkins, M. Henderson, D. McCready, G. Herman, *J. Phys. Chem. B* 105 (2001) 595–596.

[33] K. Fukuda, I. Nakai, C. Oishi, M. Nomura, M. Harada, Y. Ebina, T. Sasaki, *J. Phys. Chem. B* 108 (2004) 13088–13092.

[34] M. Osada, Y. Ebina, K. Fukuda, K. Ono, K. Takada, K. Yamaura, E. Takayama-Muromachi, T. Sasaki, *Phys. Rev. B* 73 (2006) 15.

[35] T. Kubo, A. Nakahira, *J. Phys. Chem. C* 112 (2008) 1658–1662.

[36] Y.F. Zhao, G.B. Chen, T. Bian, C. Zhou, G. Waterhouse, L.Z. Wu, C.H. Tung, L. Smith, D. O’Hare, T.R. Zhang, *Adv. Mater.* 27 (2015) 7824–7831.

[37] S. Gao, Z.T. Sun, W. Liu, X.C. Jiao, X.L. Zu, Q.T. Hu, Y.F. Sun, T. Yao, W.H. Zhang, S.Q. Wei, Y. Xie, *Nat. Commun.* 8 (2017) 14503.

[38] Z. Li, C. Xiao, H. Zhu, Y. Xie, *J. Am. Chem. Soc.* 138 (2016) 14810–14819.

[39] Y.F. Sun, Z.H. Sun, S. Gao, H. Cheng, Q.H. Liu, F.C. Lei, S.Q. Wei, Y. Xie, *Adv. Energy Mater.* 4 (2013) 1–11.

[40] X. Ding, W.K. Ho, J. Shang, L.Z. Zhang, *Appl. Catal. B: Environ.* 182 (2016) 316–325.

[41] X. Ding, K. Zhao, L.Z. Zhang, *Environ. Sci. Technol.* 48 (2014) 5823–5831.